Applied Catalysis B: Environment and Energy 387 (2026) 126479

Contents lists available at ScienceDirect

Applied Catalysis B: Environment and Energy

journal homepage: www.elsevier.com/locate/apcatb

Phase-dependent dechlorination mechanisms of organochlorines on MoS_2 electrodes: Contrasting roles of 1T and 2H phases

Beizhao Chen [a,b], Mengxia Wang [b], Aling Wan [b], Meng Zhang [b], Hanchao Zhang [d], Zhongying Wang [b,c,*], Yi Jiang [a,e,**]

[a] Department of Civil and Environmental Engineering, The Hong Kong Polytechnic University, Hung Hom, Kowloon, Hong Kong, China
[b] School of Environmental Science and Engineering, Southern University of Science and Technology, Shenzhen 518055, China
[c] Guangdong Provincial Key Laboratory of Soil and Groundwater Pollution Control, Southern University of Science and Technology, Shenzhen 518055, China
[d] School of Fashion and Textiles, The Hong Kong Polytechnic University, Hung Hom, Kowloon, Hong Kong, China
[e] State Key Laboratory of Marine Environmental Health, City University of Hong Kong, Kowloon, Hong Kong, China

ARTICLE INFO

Keywords:
Dechlorination
Direct electron transfer
Atomic hydrogen
MoS_2 electrode
DFT calculation

ABSTRACT

Organochlorine compounds (OCs), notorious for their environmental persistence and toxicity, pose significant risks to aquatic ecosystems and human health. Electrochemical dechlorination using molybdenum disulfide (MoS_2), a cost-effective and efficient material, offers a promising remediation strategy. However, the distinct mechanistic roles of the metallic (1 T) and semiconducting (2H) phases in dechlorination—whether through direct electron transfer (DET) or by atomic hydrogen (H*)—remain highly controversial and poorly understood. In this study, we elucidate phase-dependent dechlorination pathways by employing florfenicol (FLO), a refractory chlorinated antibiotic, as a model pollutant. The 2H-MoS_2 electrode achieved efficient dechlorination ($0.98\ h^{-1}$) at moderate potentials (−0.8 to −1.1 V vs. Ag/AgCl); in contrast, the 1T-MoS_2 phase required a higher potential (−1.3 V) to achieve a comparable kinetic rate constant. The performance of both electrodes is competitive with previously reported expensive precious metal electrodes. Further mechanistic investigations revealed that DET dominates on 2H-MoS_2, enabling two-step dechlorination, but 1T-MoS_2 mainly relies on the H*-mediated pathway for one-step deep dechlorination. Density functional theory (DFT) calculations corroborated these findings, revealing that the DET pathway on 2H-MoS_2 has lower energy barriers (0.53 and 1.60 eV for the first and second C–Cl bond cleavages, respectively) compared to the H* pathway (0.80 and 3.23 eV), suggesting the second C–Cl bond cleavage as the rate-limiting step. For 1T-MoS_2, the H*-mediated pathway showed lower energy barriers (2.0 and 1.53 eV, respectively), supporting one-step deep dechlorination via H*. Robust performance of MoS_2 electrodes was also demonstrated in complex water matrices and stability tests, underscoring their practical applicability. This work resolves outstanding controversies regarding dechlorination mechanisms on MoS_2 and provides a robust foundation for the further engineering of MoS_2-based materials for advanced reductive environmental applications.

1. Introduction

The increasing use and discharge of organochlorine compounds (OCs) into the natural environment pose an imminent threat to human health and the aquatic ecosystem [1]. Among these, florfenicol (FLO)—a halogenated antibiotic widely applied in veterinary and aquaculture practices—stands out for its enduring biological toxicity and environmental persistence [2]. FLO persists in water systems at concentrations ranging from 3.55 to 4610 $ng\cdot L^{-1}$ and resists conventional oxidation treatments due to its stable chlorine substituents [3–6]. This recalcitrance has driven interest in reductive remediation approaches capable of cleaving the carbon–chlorine bond, including Pd/H_2 catalytic hydrogenation [7,8], $NaBH_4$ reduction [9], zero-valent iron-based reduction [10,11], biological reduction [12], and electrocatalytic hydrogenation (ECH) [13–15]. Among these, ECH presents a particularly promising sustainable approach, requiring no chemical additives while effectively treating high concentrations of OCs. However, the practical implementation of ECH is hampered by limitations of the

---

* Corresponding author at: School of Environmental Science and Engineering, Southern University of Science and Technology, Shenzhen 518055, China.
** Corresponding author at: Department of Civil and Environmental Engineering, The Hong Kong Polytechnic University, Hung Hom, Kowloon, Hong Kong, China.
E-mail addresses: wangzy6@sustech.edu.cn (Z. Wang), yi-cee.jiang@polyu.edu.hk (Y. Jiang).

https://doi.org/10.1016/j.apcatb.2026.126479
Received 2 January 2026; Accepted 24 January 2026

currently available electrocatalysts, which often suffer from high cost, poor efficiency, and low selectivity towards nontoxic products. The development of cost-effective, high-performance ECH electrocatalysts is therefore crucial for unlocking the full potential of ECH for organochlorine remediation.

Molybdenum disulfide (MoS_2) derived from molybdenite mines is a cost-effective material with diverse applications [16–19]. The exceptional activity of MoS_2-based catalysts stems from their unique layered structure, where Mo atoms are bonded to S atoms within layers held together by weak van der Waals forces. MoS_2 exhibits different structural phases, notably the metallic 1 T phase and the semiconducting 2H phase. The exposed edge sites of MoS_2 enable efficient reactant adsorption and reduction reactions. Leveraging these attributes, MoS_2-based catalysts have been widely explored in various electrocatalytic applications such as H_2 evolution reaction (HER) [17,20,21], carbon dioxide reduction [22–24], oxygen evolution/reduction [25–27], nitrate reduction [18,28], and nitrogen fixation [29,30]. In these processes, atomic hydrogen (H*)—abundantly generated on MoS_2 surfaces—plays a central role, and its formation is strongly influenced by the MoS_2 phase. Notably, the metallic 1 T phase exhibits superior H* generation capability compared to the 2H phase, thereby offering enhanced catalytic performance [30].

Recently, MoS_2 has also emerged as a promising electrocatalyst for dechlorination due to its extensive adsorption sites and its dual capacity for facilitating electron transfer and generating H*. For example, Huang et al. demonstrated efficient trichloroacetic acid (TCAA) dechlorination using MoS_2 nanosheets, with further improvements achieved through transition metal doping [31]. Similarly, cobalt-doped MoS_2 electrodes exhibited high degradation efficiencies for halogenated disinfection byproducts, with catalytic enhancement linked to accelerated HER kinetics and increased H* production (i.e., the Volmer step of HER) [32]. Moreover, Jiang et al. revealed that ultrathin MoS_2 nanosheets achieved reaction rates 4.1- and 28-fold higher than the commercial MoS_2 and carbon paper, respectively [33]. Collectively, these studies highlight the potential of MoS_2-based materials for dehalogenation applications.

Despite these advances, several critical knowledge gaps remain. First, the mechanistic pathways underlying electrocatalytic dechlorination on MoS_2 are not fully understood. Dechlorination can proceed via direct electron transfer (DET), in which adsorbed OCs undergo C−Cl bond cleavage to form radicals and subsequently anions, or via H* reduction, where surface-generated H* hydrogenates the adsorbed OCs. However, the effective utilization of H* is often hampered by the competing HER, in which H* recombines to form H_2 gas. This not only lowers dechlorination efficiency and Faradaic efficiency but also potentially disrupts mass transfer due to gas bubbling. This paradox is particularly pronounced for the 1 T phase of MoS_2; while it provides superior conductivity and higher H* generation, it may simultaneously facilitate HER to a greater extent. To date, no systematic studies have examined the dechlorination performance of 1T-MoS_2, and the interplay between H* generation/reduction, DET, and HER suppression across different MoS_2 phases remains poorly understood. Previous research has predominantly focused on the semiconducting 2H phase, largely attributing dechlorination activity to H* reduction [31,32]. However, the observation that dechlorination is only mildly inhibited in the presence of H* scavengers strongly suggests a significant concurrent role for DET. Although the strong reducing potential of H* (−2.10 V vs. SHE [34,35]) is considered crucial for cleaving recalcitrant C–Cl bonds, it remains unknown whether DET alone can achieve complete dechlorination of multi-chlorinated OCs, or if H* is indispensable for the final C−Cl cleavage steps. Therefore, elucidating the distinct roles of the 1 T and 2H phases and their dominant dechlorination pathways (DET vs. H*) is critical for the rational design of more efficient MoS_2 catalysts.

To address the knowledge gaps, the present study systematically investigates the mechanistic roles of both 1T- and 2H-MoS_2 phases in the electrochemical dechlorination of FLO, integrating experimental and computational approaches to provide molecular-level and thermodynamic insights. We first evaluate the degradation and dechlorination performance of FLO on both MoS_2 phases under varying electrical potentials, determining their respective Faradaic efficiencies and elucidating performance differences through comprehensive electrochemical characterization. The contributions of DET and H* pathways are further dissected using H* quenching experiments, electron paramagnetic resonance (EPR) detection of H*, and semi-quantitative analysis of reaction intermediates by HPLC-MS. Importantly, density functional theory (DFT) calculations provide thermodynamic and kinetic insights by mapping the energy barriers and free energy changes associated with different dechlorination pathways. Finally, the practical applicability of MoS_2 electrodes is assessed under environmentally relevant conditions, including variations in initial pH, natural organic matter (NOM), dissolved oxygen (DO), and long-term cycling stability. Collectively, these results clarify the mechanistic basis of MoS_2-mediated dechlorination and provide a robust foundation for the further engineering of MoS_2-based materials for advanced reductive environmental applications.

2. Materials and methods

2.1. Chemicals and materials

FLO, Na_2SO_4, $(NH_4)_6Mo_7O_{24}•4H_2O$, CH_3CSNH_2, tertiary butanol (t-BuOH), MeOH, and Nafion 117 solution (5 wt%) were purchased from Macklin Reagents (Shanghai, China). 5,5-Dimethyl-1-pyrroline-N-oxide (DMPO, 98 %) was obtained from TCI Chemical Industry Development Co. Ltd (Shanghai, China). All chemicals were used as received without additional purification, and the solutions were prepared with ultrapure water (Milli-Q, Direct8, Millipore).

2.2. Synthesis of MoS_2 electrodes

The synthesis of MoS_2 electrodes in different phases was conducted using the hydrothermal method (Fig. S1) [30,36–40]. The procedure involved the addition of 0.55 g of ammonium molybdate, 0.47 g of thioacetamide, and 20 mL of water into a 50 mL Teflon-lined autoclave, with a S:Mo molar ratio of 2:1. A 2×2 cm^2 carbon paper (CP) substrate was immersed in the solution and ultrasonicated for 1 h. Subsequently, the assembly was subjected to a 240 ℃ treatment in an oven for 24 h. After natural cooling, the CP coated with 2H-MoS_2 was rinsed with pure water and dried at 70 ℃ for future utilization, yielding the 2H-MoS_2 electrode. The 1T-MoS_2 electrode was produced using the same procedure but with hydrothermal treatment at 180 ℃ for 12 h.

2.3. Electro-reductive dechlorination of FLO

Electro-reductive dechlorination of FLO was performed in a dual-compartment H-type electrochemical cell (50 mL per chamber) separated by a Nafion-117 (DuPont) proton exchange membrane and connected to a CHI-760E electrochemical workstation or a DC power (Fig. S2). For a typical electro-reduction process, the prepared MoS_2 electrode functioned as the working electrode, with a platinum foil (10 × 10 mm) serving as the counter electrode, and an Ag/AgCl electrode (3.0 M KCl) acting as the reference electrode. Each chamber of the cell contained 40 mL of 100 mM Na_2SO_4 electrolyte solution, with FLO added to the catholyte at an initial concentration of 20 mg/L. A magnetic stirring at 300 rpm was applied to facilitate mixing. Electrolysis was conducted either under constant potential through the amperometric I-t technique or at fixed voltage using a DC power supply. At predetermined intervals, 0.8 mL of the cathodic solution was withdrawn and filtered using a 0.22 μm syringe filter (PES, JIN TENG) for subsequent chemical analysis (Text S1).

For quenching experiments, 5−100 mM TBA was added to the catholyte prior to electrolysis (Text S2). The NOM interference was assessed by adding 2 or 6 mg/L of NOM into the solution. To study the

DO effect, air or N_2 was bubbled into the H-cell cathode chamber to reach DO concentrations of 5.5 mg/L (air) or 0.45 mg/L (N_2); DO concentrations pre- and post-reaction were monitored. The initial solution pH was adjusted using 0.1 M H_2SO_4 or NaOH aqueous solution as necessary. To ensure accuracy and consistency, all experiments were conducted at least twice to ensure reproducibility.

2.4. Cathode characterization

Scanning electron microscopy (SEM; Merlin, ZEISS) was used to examine the morphologies and structures of the cathode. The HAADF-STEM measurements were carried out on a JEOL JEM-ARM300F field-emission transmission electron microscope operated at an accelerating voltage of 200 kV to obtain atomic-resolution images and elemental distribution. The crystal structure and chemical compositions were characterized using X-ray diffraction (XRD; Smartlab, Rigaku) with Cu Kα radiation ($\lambda = 1.5406$ Å). X-ray photoelectron spectroscopy (XPS) was recorded on a PHI 5000 Versaprobe system with monochromatic Al Kα radiation, and all binding energies were referenced to the C 1 s peak at 284.8 eV. Raman spectroscopy was conducted using a Renishaw InVia Reflex Raman microscope, scanning from 300 to 600 cm^{-1} with excitation provided by a 532 nm laser. Thermogravimetric analysis (TGA) was performed using a Waters thermogravimetric analyzer (TGA550), with the temperature ramped from 25 to 600 °C. Electron paramagnetic resonance (EPR) measurements were performed using a Bruker EMX PLUS instrument (Text S3). Fourier transform infrared spectroscopy (FTIR) was conducted with a Bruker Vertex 70 v spectrometer equipped with an ATR detector.

2.5. Electrochemical measurements

To evaluate the electrochemical properties of the fabricated MoS_2 electrode materials, several characterization techniques were applied using a standard three-electrode cell system. The measurements included electrochemically active surface area (ECSA), electrochemical impedance spectroscopy (EIS), cyclic voltammetry (CV), and linear sweep voltammetry (LSV). The experimental setup featured a Pt wire as the counter electrode, the prepared MoS_2 electrode functioned as the

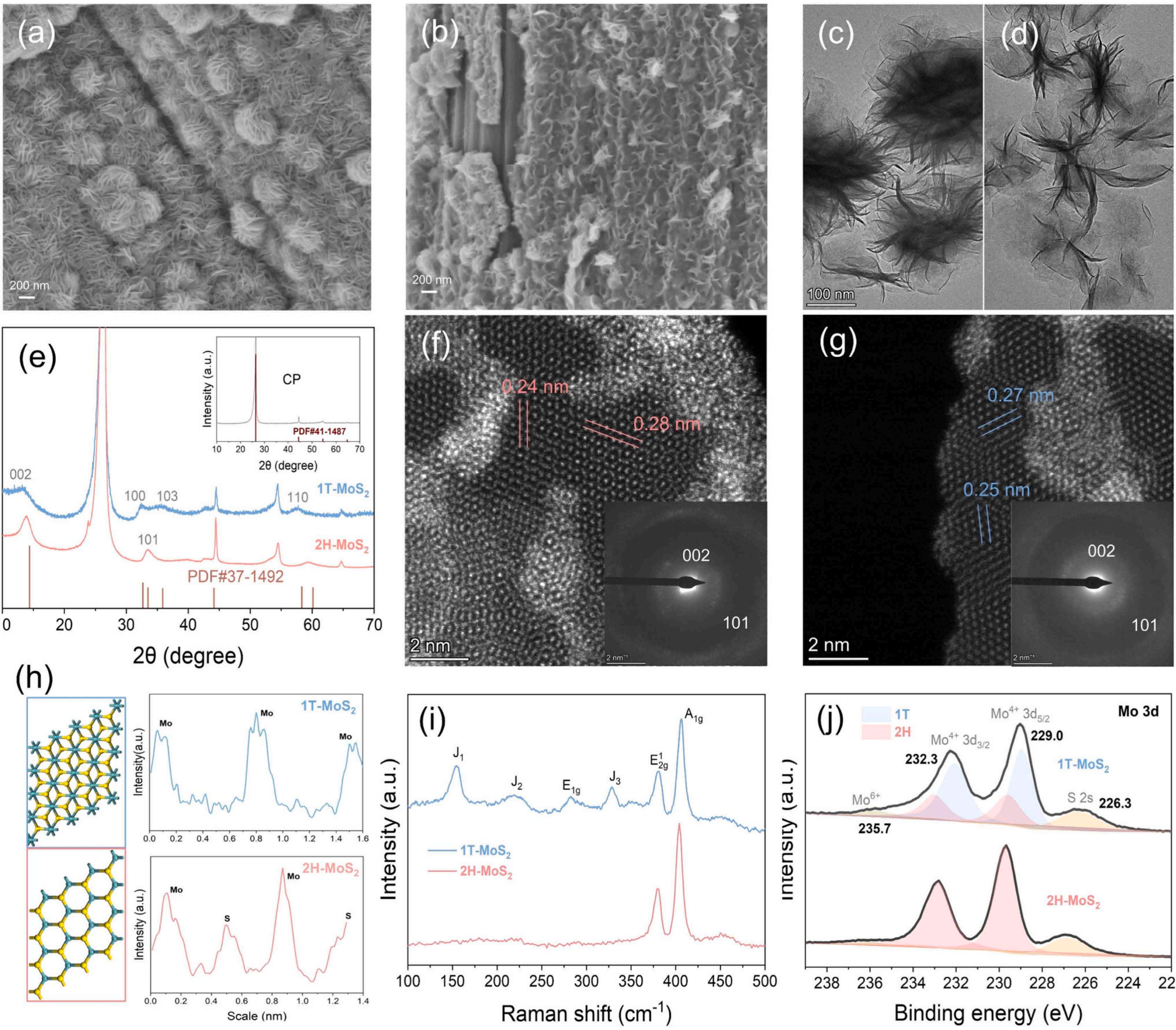

Fig. 1. Characterization of 1T- and 2H-MoS_2 electrodes: (a) SEM images of 1T-MoS_2 and (b) 2H-MoS_2 grown on carbon papers; TEM images display silky ultrathin sheet morphology of (c) 2H-MoS_2 and (d)1T-MoS_2. (e) XRD pattern of 1T- and 2H-MoS_2 electrodes. HAADF-STEM image and corresponding SAED pattern (insert image) of (f) 2H-MoS_2 and (g)1T-MoS_2; (h) The atomic intensity of Mo and S in 1T- and 2H-MoS_2 indicated in Fig. 1f and 1g, respectively. (i) Raman spectra; and (j) high-resolution XPS (HRXPS) analysis of both phases.

working electrode, Ag/AgCl as the reference electrode, and 100 mM Na_2SO_4 as the electrolyte. ECSA was determined at scan rates ranging from 20 mV/s to 100 mV/s within the non-faradaic range of applied potential. EIS measurements involved a 5 mV voltage with a frequency range from 0.01 Hz to 10 kHz. CV and LSV were performed between −1.2 and 0.4 V (vs Ag/AgCl) at a scan rate of 50 mV/s.

2.6. DFT calculations

First-principles DFT calculations were conducted using the CASTEP package with a plane wave basis [41]. The calculation details can be found in Text S4, Supporting Information.

3. Results and discussion

3.1. Structural and electrochemical characterization of the MoS_2 electrodes

Flower-like MoS_2 nanosheet arrays of consistent size and mass loading were directly grown on CP substrates to fabricate the electrodes (Fig. 1 and S3) [30]. Both 1T- and 2H-MoS_2 electrodes exhibited similar mass loadings of approximately 4.5 mg (Fig. S3). In contrast to the smooth surface of the blank CP electrode (Fig. S4), the MoS_2 electrodes exhibited a roughened surface adorned with vertically oriented nanosheets, signifying successful growth of MoS_2 on the CP substrate. Specifically, the 2H-MoS_2 electrode presents a more airy and uniform morphology (Fig. 1a, c), while 1T-MoS_2 electrode reveals a densely packed, silky stacked nanosheet structure (Fig. 1b, d). X-ray diffraction (XRD) analysis confirms the structural identity of the synthesized 1T- and 2H-MoS_2 electrodes (Fig. 1e). The observed diffraction patterns correspond well with standard ICDD references (PDF#37–1492 for MoS_2 and PDF#41–1487 for the carbon paper substrate). For the 1T-MoS_2 phase, characteristic diffraction peaks appear at $2\theta = 13.4^\circ$, 32.4°, and 35.6°, corresponding to the (002), (100), and (103) planes. These reflections indicate an interlayer spacing of ∼0.66 nm and in-plane D-spacings of ∼0.28 nm and ∼0.25 nm, respectively. In contrast, the 2H-MoS_2 phase exhibits analogous peaks at 13.9° (002) and 33.5° (101), which correspond to a smaller interlayer spacing of ∼0.64 nm and an in-plane D-spacing of ∼0.27 nm. These values are in agreement with direct measurements from HRTEM imaging (Fig. S5), which show interlayer/in-plane spacings of ∼0.65/0.28 nm for the 1T phase and ∼0.64/0.27 nm for the 2H phase. The expanded interlayer spacing in the 1T phase (∼0.66 nm versus ∼0.64 nm for the 2H phase), commonly attributed to lattice expansion or intercalation [30]. Furthermore, while the 2H phase is distinguished by a sharp, well-defined (101) peak at 33.5° indicative of high crystallinity, this characteristic peak is significantly weakened and broadened in the 1T phase, consistent with its structural distortion or tendency toward amorphization. Taken together, these distinct XRD and HRTEM signatures conclusively verify the successful synthesis of both MoS_2 phases with their unique crystal structures.

To unambiguously differentiate the 1 T and 2H phases, we employed a suite of complementary characterization techniques, with atomic-resolution HAADF-STEM providing the most definitive identification. This method directly resolves the distinct in-plane interplanar spacings of the (100) and (103) planes, yielding values of 0.27/0.25 nm for 1T-MoS_2 and 0.28/0.24 nm for 2H-MoS_2, in agreement with XRD analysis and confirming high crystallinity. Crucially, HAADF-STEM imaging reveals a key structural hallmark: the S atomic column intensity is markedly suppressed in the octahedral 1 T phase, contrasting sharply with the bright intensity in the trigonal prismatic 2H phase. This contrast is quantified in the intensity profiles (Fig. 1f, 1h), where 1T-MoS_2 shows a dominant Mo peak with attenuated S signals, while 2H-MoS_2 displays well-resolved, alternating Mo and S peaks—a direct visualization of their distinct lattice symmetries. Selected-area electron diffraction (SAED) identifying facets such as (002) and (101) or (100) provides additional structural identification.

The full-range XPS survey spectra (Fig. S6, Table S1) confirm the elemental surface composition, dominated by Mo and S. Minor C and O signals originate from the mounting resin and surface oxidation, respectively. No nitrogen is detected, indicating high-purity MoS_2. This result is further supported by TEM-EDS elemental mapping (Fig. S7). The deconvoluted XPS spectra unveiled the intricate phase composition of the MoS_2 materials in their initial state. The Mo 3d spectrum of the 2H-MoS_2 sample consists of peaks at ∼228.7 eV and 232.0 eV, corresponding to Mo^{4+} $3d_{5/2}$ and $3d_{3/2}$ components of the 2H phase (Fig. 1d). A minor Mo^{6+} contribution is also observed and is attributed to surface oxidation [42,43]. An additional doublet at 227.8 and 231.0 eV was discernible, signifying the presence of the 1T phase. The proportion of the 1T phase was determined to be 72.5 %, aligning closely with prior findings [37,38]. In the Raman spectrum of 2H-MoS_2 (Fig. 1c), two distinct vibration peaks were identified at 375 and 403 cm^{-1}, corresponding to the in-plane Mo−S phonon mode (E^1_{2g}), and out-of-plane Mo−S mode (A_{1g}), respectively [30,36]. In contrast, the 1T-MoS_2 sample exhibited additional bands at 154, 219, 282, and 329 cm^{-1}, associated with J_1, J_2, E_{1g}, and J_3 modes of the 1T phase [28]. The presence of both 1 T and 2H-related peaks implies a mixed-phase composition, which is typical given the high formation energy and inherent thermodynamic instability of 1T-MoS_2 [44]. TGA analysis reveals distinct thermal behaviors (Fig. S8). 1T-MoS_2 shows 18 % mass loss to 600°C from water release, phase transition, and decomposition. In contrast, 2H-MoS_2 is stable with only ∼2 % loss, further underscoring their structural difference.

To explore the electrochemically active sites and properties of the fabricated MoS_2 electrodes, the ECSA was assessed by measuring double-layer capacitance (C_{dl}) [45]. The C_{dl} of 1T-MoS_2 was found to be 82.23 μF/cm^2, markedly exceeding 54.03 μF/cm^2 of the 2H-MoS_2 (Fig. 2a and Fig. S9), indicating a substantially higher density of electrochemically accessible sites. Additionally, the EIS measurements were conducted to examine the role of charge transfer resistance (R_{ct}) in the two MoS_2 material phases (Fig. 2b). The R_{ct} of 1T-MoS_2 was slightly lower than that of 2H-MoS_2, indicating its higher conductivity than 2H-MoS_2. However, it is important to note that while EIS effectively probes overall charge transfer kinetics, it cannot distinguish the specific electrochemical pathways for different reactions. In this system, the competitive HER and electroreductive dechlorination occur at similar surface sites, and the measured R_{ct} reflects a general charge mobility beneficial to both processes. Accordingly, the LSV curves for 1T-MoS_2 and 2H-MoS_2 nanosheets were collected to assess their activity towards the competing HER (Fig. 2c). The 1T-MoS_2 showed a lower hydrogen evolution potential than 2H-MoS_2. Furthermore, based on the intercept of the linear region in the Tafel plots [17,46], the exchange current density (j_0) for HER over 2H-MoS_2 was calculated to be 402.3 mV/dec, which was higher than that (152.0 mV/dec) over 1T-MoS_2 (Fig. 2d). Consequently, the HER activity on 2H-MoS_2 was much lower compared to the 1T-MoS_2 electrode. These results are consistent with those in the literature that the 1T-MoS_2 has higher electrical conductivity and HER activity compared to 2H-MoS_2.

3.2. Electroreduction of FLO on the 1T-/2H-MoS_2 electrodes

FLO was selected as a model compound to assess the electroreductive dechlorination performance of the MoS_2 electrodes. Control experiments without applied potential showed that MoS_2 achieved approximately 20 % adsorption of FLO, higher than the 12 % observed with the blank CP electrode (Fig. S10), indicating enhanced adsorption capacity and potential adsorbate-surface interactions on MoS_2. Subsequently, FLO dechlorination experiments were performed over a range of applied potentials from −0.6 to −1.3 V vs Ag/AgCl, and the resulting degradation kinetics were fitted using a first-order model (Fig. 3a, Fig. S11-S12, and Text S5). The CP electrode exhibited sluggish FLO reduction, with rate constants of 0.09 −0.20 h^{-1}. In contrast, the 1T-

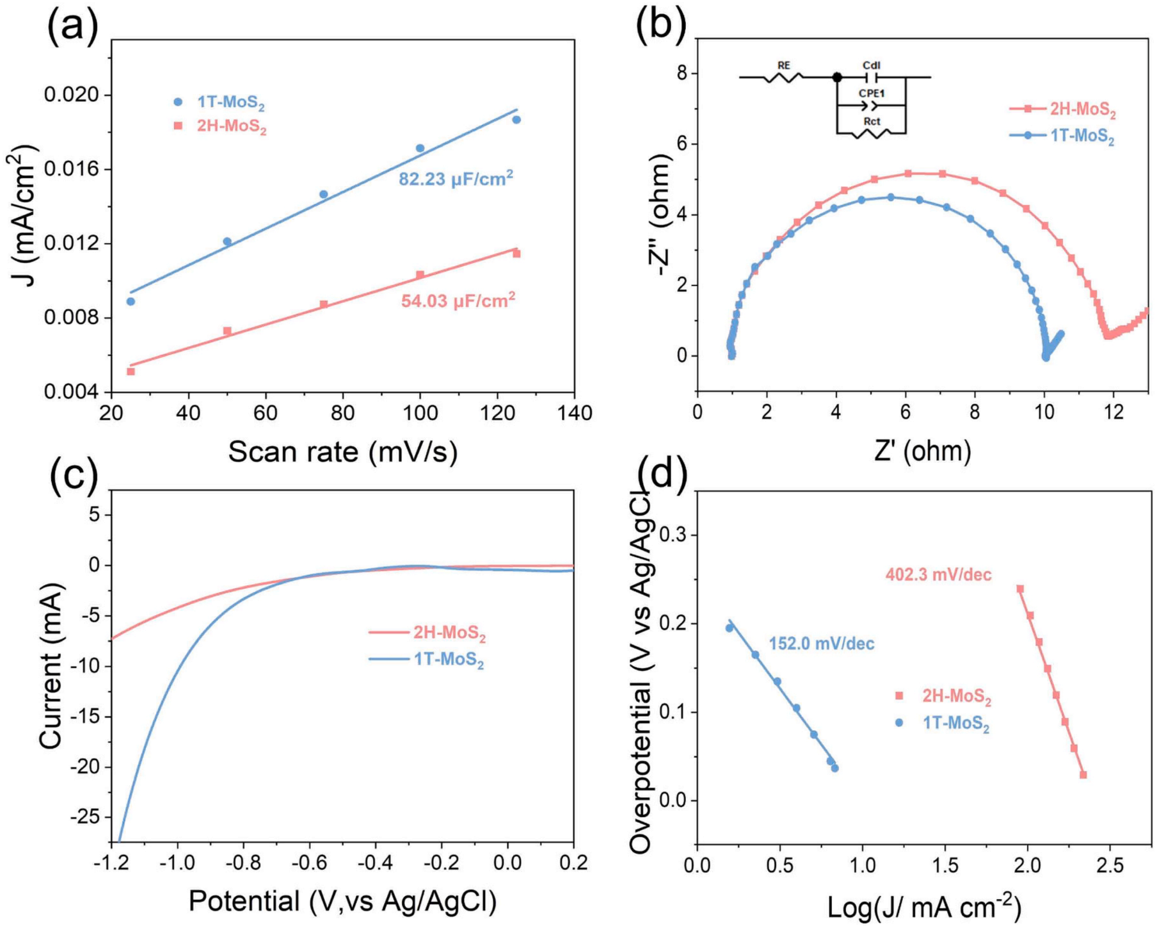

Fig. 2. Electrochemical characterization of 1T- and 2H-MoS_2 electrodes in 0.1 M Na_2SO_4 electrolyte: (a) ECSA, (b) EIS Nyquist plot, (c) LSV curves, and (d) corresponding Tafel plots.

MoS_2 electrode demonstrated significantly enhanced FLO degradation, with reaction rate constants increasing from 0.11 h^{-1} at −0.6 V to 1.04 h^{-1} at −1.3 V. A particularly sharp increase occurred between −1.1 and −1.2 V (k from 0.46 to 0.97 h^{-1}), indicating a potential-dependent activation threshold. For the 2H-MoS_2 electrode, the reaction rate constant peaked at 0.98 h^{-1} at −1.1 V, then declined slightly at more negative potentials. These values are comparable to those reported in the literature (e.g., 0.0135 min^{-1} under −1.2 V at 2H MoS_2).[32] A substantial increase occurred earlier, between −0.7 and −0.8 V (k from 0.24 to 0.56 h^{-1}), correlating with a rise in current, evidenced from the CV data as shown later, which signifies the onset of electron-mediated reduction. Notably, at potentials below −1.1 V, the 2H-MoS_2 electrode exhibited markedly higher rate constants than both the CP and 1 T electrodes.

Chloride release profiles (Fig. 3b–d) corroborated the degradation trends. The CP electrode was largely ineffective, achieving only 10 % dechlorination at −1.2 V after 4 h, whereas 2H-MoS_2 and 1T-MoS_2 electrodes reached ~85 % and ~90 % efficiency (Text S6), respectively. The 1 T phase required a more negative potential (−1.3 V) for optimal performance. This was consistent with the chlorine mass balance, which showed the CP electrode retained over 50 % of its organic chlorine with minimal Cl^- release (Fig. S11c). While both MoS_2 electrodes facilitated deeper dechlorination than CP, their performance was highly potential-dependent (Fig. 3e-f). The 1T-MoS_2 electrode demonstrated a sharp, potential-activated transition. At moderate potentials (−0.6 to −1.1 V), the system was characterized by low Cl^- release (10–35 %) and significant adsorption (~10–25 %). In contrast, applying potentials beyond −1.1 V triggered a switch to deep dechlorination, yielding over 85 % Cl^- release (Fig. 3e). Conversely, the 2H-MoS_2 electrode achieved efficient deep dechlorination at lower potentials. Across the −0.8 to −1.2 V range, it consistently released over 80 % of chlorine while the adsorbed species remained below 5 %, demonstrating a sharper and more complete conversion. The divergent dechlorination profiles underscore a fundamental performance difference: 2H-MoS_2 is highly effective at low potentials but loses efficacy at higher ones, whereas 1T-MoS_2 activates effectively only beyond the −1.1 V threshold, a behavior largely attributed to the suppression by the competing HER.

To investigate the site-normalized dechlorination activity of the 1 T and 2H phases, the turnover frequency (TOF) was calculated based on ECSA and FLO degradation performance (Text S7 and Fig. S13). The results indicate that the TOF of the 2H phase is higher than that of the 1 T phase, which could be attributed to the significant competition from the HER in the 1 T phase. This difference results in variations in dechlorination performance under different applied potentials. The Faradaic efficiency (FE) further underscores the superiority of the two phase MoS_2 electrodes (Text S8, Fig. 3e, f). While the CP electrode maintained a low FE (<0.5 %) at all potentials, the MoS_2 variants performed significantly better. The 1T-MoS_2 electrode reached a peak FE of ~2.11 % at −0.9 V, while the 2H-MoS_2 electrode achieved the highest FE of ~3.3 % at −0.8 V before declining. The higher FE of 2H-MoS_2 at a lower potential compared to 1T-MoS_2 suggests differences in their FLO dechlorination mechanisms.

The FLO dechlorination was evidenced by the changes in the C−Cl bonds in the FTIR spectra (Fig. S14). At −0.8 V, the C−Cl bond vibrations (600 −650 cm^{-1}) [47,48] nearly disappeared for 2H-MoS_2 but persisted on 1T-MoS_2 over a four-hour reaction period, indicating more

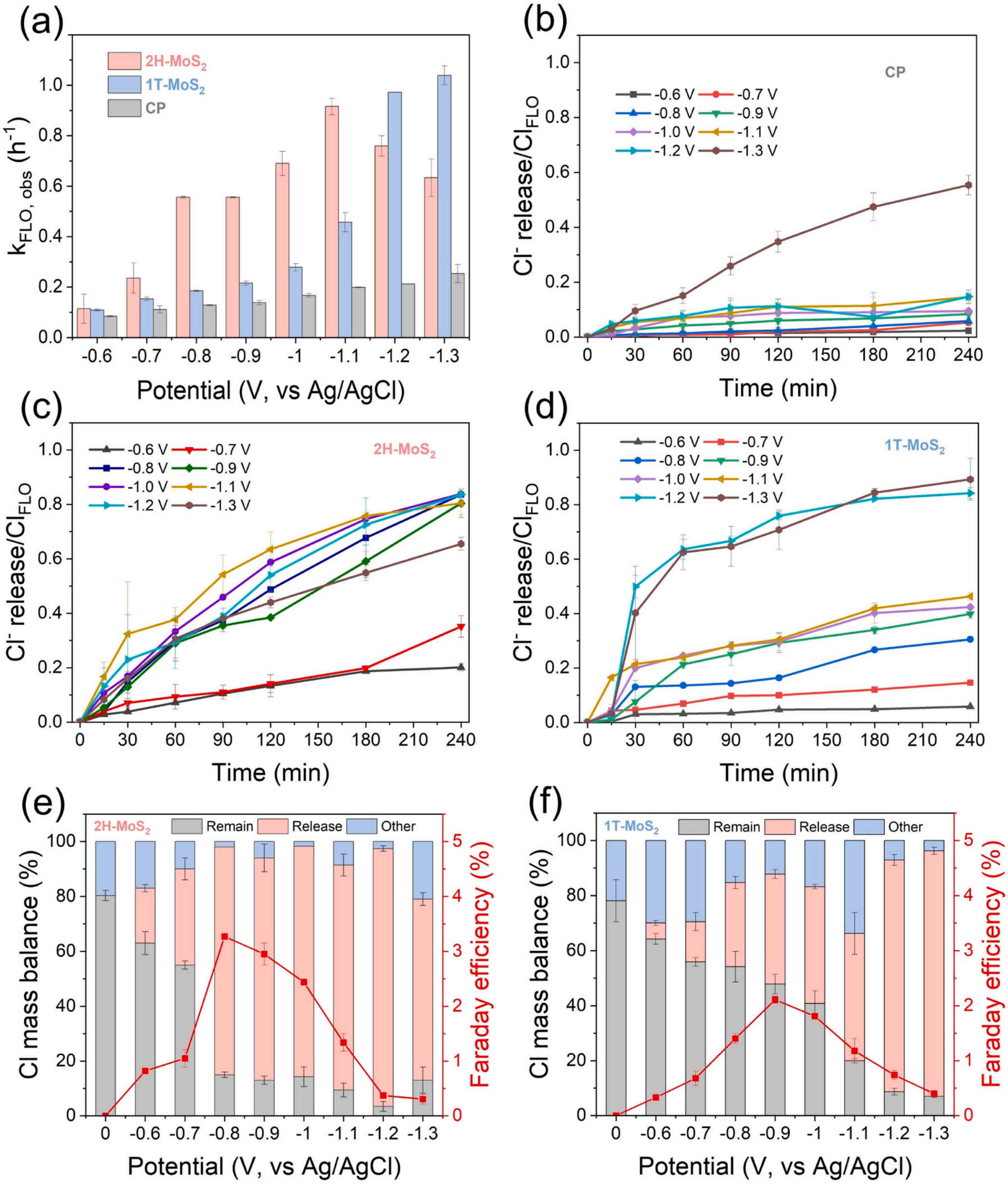

Fig. 3. Performance of 1T-/2H-MoS_2 and CP electrodes for FLO reduction at various applied potentials. (a) Comparison of FLO degradation kinetics. (b-d) Chloride (Cl^-) release on (b) bare carbon paper (CP), (c) 2H-MoS_2, and (d) 1T-MoS_2 electrodes. (e, f) Chlorine mass balance and faradaic efficiency (FE) analysis after a 4-hour reaction on (e) 2H-MoS_2 and (f) 1T-MoS_2. Experimental conditions: [FLO] = 20 mg/L, [Na_2SO_4] = 100 mM, initial pH 5.8.

selective dechlorination of FLO at low potentials on the 2H electrode. This is consistent with its lower HER activity, allowing more electrons to be directed toward FLO reduction (Fig. 2c, d). At potentials more negative than −1.1 V, the formation of H_2 bubbles at 2H-MoS_2 was obvious (see Fig. S15), which subsequently impeded the mass transport of FLO molecules onto the electrode surface, leading to a decrease in the reduction rates [33]. In contrast, the 1T-MoS_2 electrode favored the HER over FLO reduction at low potentials, as indicated by its lower Tafel slope (Fig. 2d). This competition from the HER explains its lower FLO degradation kinetics.

3.3. Mechanistic insights into FLO dechlorination at the 1T- and 2H-MoS_2 electrodes

To explain the disparity in dechlorination performance between the 1T- and 2H-MoS_2 electrodes, TBA was first used as a probe to assess the involvement of H* in the reduction process [13,15,49]. The FLO degradation rate constants at different TBA concentrations were compared between 2H- and 1T-MoS_2 electrodes (Fig. 4a and S16). The 2H-MoS_2 exhibited a high FLO degradation rate constant, with only a 16 % reduction from 1.25 h^{-1} without TBA addition to 1.05 h^{-1}at 100 mM TBA. This mild reduction was similarly observed in a previous study, where a 17 % reduction in the removal efficiency of FLO was observed with the addition of 5 mM TBA. In contrast, at the 1T-MoS_2 electrode, the rate constants notably dropped from 1.03 h^{-1} without TBA to 0.46 h^{-1} at 100 mM TBA, a 55 % reduction. The TBA addition minimally impacted FLO dechlorination on the 2H-MoS_2 electrode (Fig. 4b), with Cl^- release decreased from 93 % at 0 mM TBA to 78 % at 100 mM TBA. However, for the 1T-MoS_2 electrode (Fig. 4c), the Cl^- release decreased from 89 % to 55 % for the same TBA concentration change. These results underscore the greater involvement of H* in FLO dechlorination on the 1T-MoS_2 electrode compared to the 2H-MoS_2 electrode. The presence and role of H* were further validated through EPR spectroscopy [13,30,49]. The DMPO_H* signal intensity in the presence of the 1T-MoS_2 electrode surpasses that of the 2H-MoS_2 electrode (Fig. 4d). Moreover, the H* intensity decreased for both phases upon FLO addition, indicating H*'s involvement in FLO reduction, particularly on the 1 T phase. Essentially, the 2H phase primarily operates through a DET mechanism, while the 1 T phase mainly involves H*-based mechanisms.

CV was performed at different FLO concentrations to monitor changes in the H_2/H* signature peak, thereby probing the proton consumption associated with either the DET or H* mechanism during electroreduction (Fig. 4e, f). For the 1T-MoS_2 electrode, as the FLO concentration increased, the H_2 production peak around −0.8 V gradually decreased (Fig. 4f). This decrease suggested FLO introduction consumed H* on the electrode surface, reducing H_2 production [50]. Conversely, for the 2H-MoS_2 (Fig. 5e), adding FLO led to a gradual decrease and negative shift of the peak related to proton adsorption near −0.4 V [13,51]. This shift highlights a strong interaction between FLO and the adsorption sites on the 2H-MoS_2 electrode, leading to FLO occupation instead of H^+ [52]. This is supported by a higher adsorption energy of FLO (−5.47 eV) compared to H^+ (−4.01 eV) from the DFT calculations, which will be discussed in the latter section.

3.4. Deep dechlorination pathways of FLO at the 1T- and 2H-MoS_2 electrodes

To assess the degree of deep dechlorination of FLO on the two MoS_2 electrodes, intermediates and products with one or two chlorine atoms detached, denoted as FLO-Cl and FLO-2Cl respectively, were monitored. Fig. S17 shows that $C_{12}H_{15}ClFNO_4S$ (FLO-Cl, $m/z = 324.0483$) and $C_{12}H_{16}FNO_4S$ (FLO-2Cl, $m/z = 289.0749$) can be clearly detected by LC-MS. The peak areas in the LC-MS spectra representing FLO-Cl and FLO-2Cl at potential range from −1.0 to −1.4 V were presented (Fig. 5b-c and Fig. S18). On the 1T-MoS_2 electrode, FLO-2Cl prevailed over the reaction time of 3 h across all potentials (−1.0 to −1.3 V). Notably, the amount of FLO-2Cl increased significantly with rising potential, while the amount of FLO-Cl remained low, showing an initial rise followed by a decline. The existence of only a very low concentration of FLO-Cl suggests an H* reduction mechanism driving one-step deep dechlorination from FLO to FLO-2Cl at the 1T-MoS_2 electrode. Initially, at lower potentials (< −1.1 V), a substantial portion of electrons was consumed for H_2 production, constraining the availability of H* for FLO reduction. Only as the current increases with the potential do the surplus H* become available for FLO reduction. Conversely, the 2H-MoS_2 electrode exhibited distinct stepwise FLO dechlorination. The amount of FLO-Cl reached a high level comparable to FLO-2Cl. The FLO-Cl content increased until ca. 30 min and then gradually declined over time. The ratio of FLO-Cl to FLO-2Cl decreased with rising potential. Interestingly, at −1.3 V, the production of FLO-Cl was minimal, indicating a transition from stepwise DET processes to a one-step DET process on the 2H-MoS_2 electrode.

Additionally, the LC-MS analysis identified FLO-2Cl-F ($C_{12}H_{17}NO_5S$, $m/z = 286.0754$) as a defluorination product, with its yield increasing at higher applied potentials on both MoS_2 electrodes (Fig. S19). This finding is corroborated by fluoride release data (Fig. S20). At lower potentials (−0.8 to −1.1 V), defluorination resembles dechlorination in that the 2H phase shows higher activity than the 1 T phase. However, a key divergence is observed in the potential-dependent trend: for

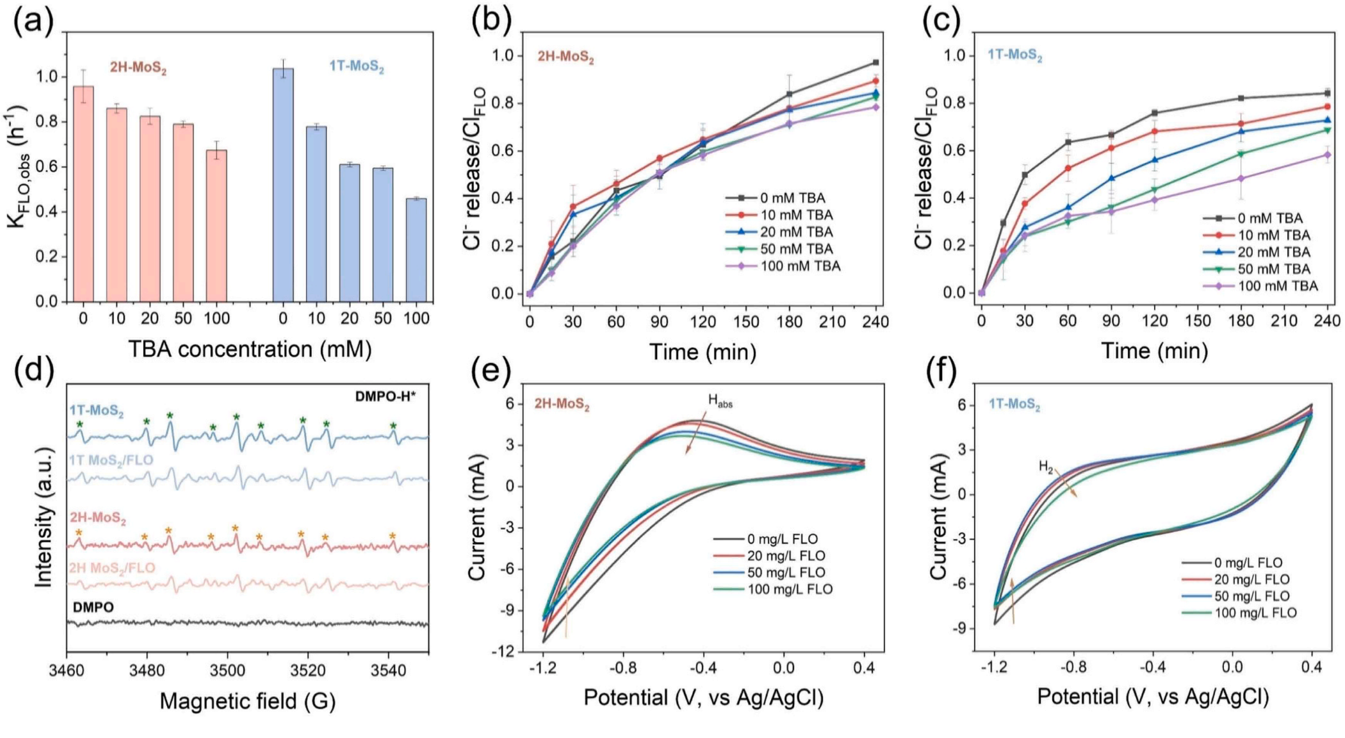

Fig. 4. Elucidating the dechlorination mechanisms of FLO on 1T- and 2H-MoS_2 electrodes. (a-c) Effect of TBA concentration (0–100 mM) on (a) FLO degradation and Cl^- release kinetics on (b) 2H-MoS_2 and (c) 1T-MoS_2. (d) EPR analysis confirming the generation of H* on both phases. (e, f) Cyclic voltammograms (CV) of (e) 2H-MoS_2 and (f) 1T-MoS_2 with varying FLO concentrations. Reaction conditions: [FLO] = 20 mg/L, [Na_2SO_4] = 100 mM, potential = -1.2 V vs. Ag/AgCl, $pH_0 = 5.8$.

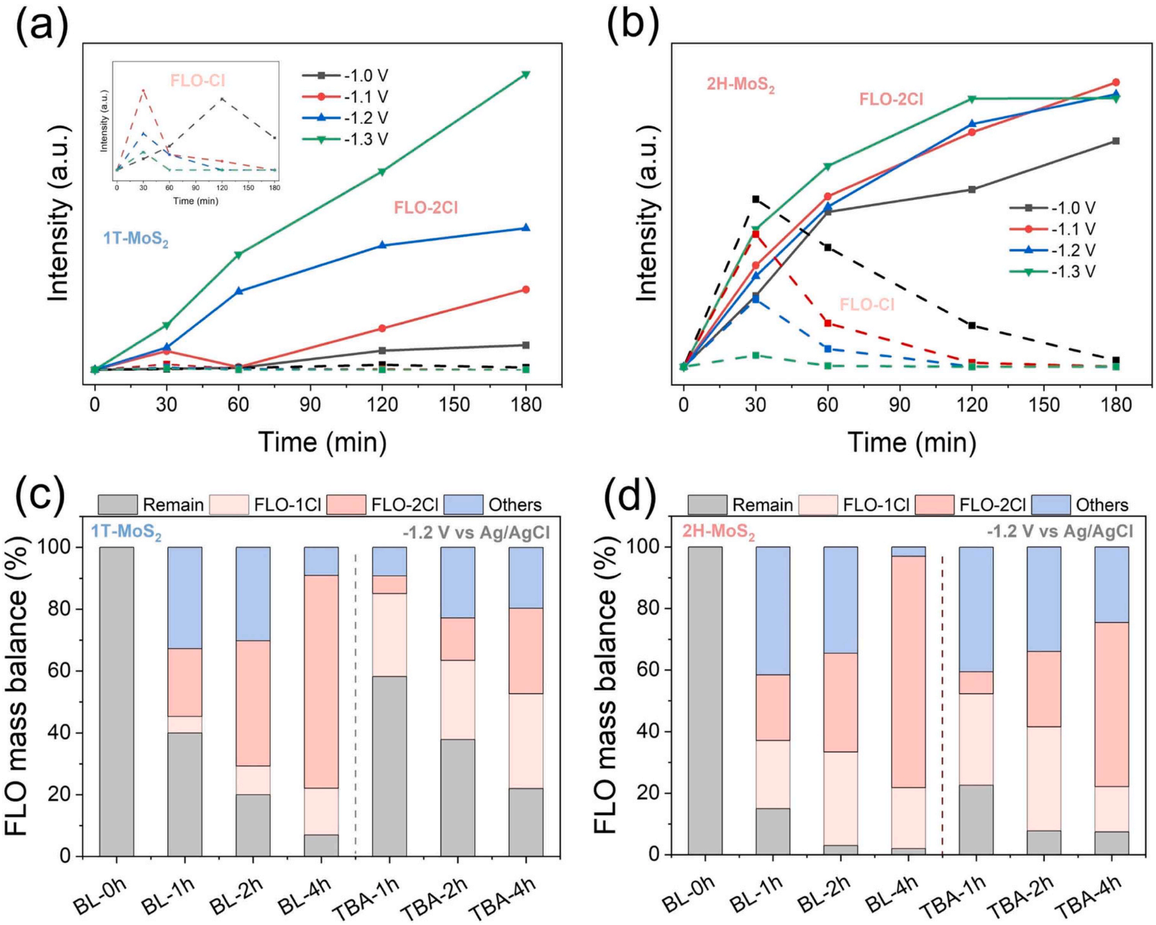

Fig. 5. Mass balance analysis of FLO dechlorination on 1T- and 2H-MoS$_2$ electrodes. (a, b) Influence of applied potential on product distribution for (a) 1T-MoS$_2$ and (b) 2H-MoS$_2$. (c, d) Variation in mass balance with and without 100 mM TBA for (c) 1T-MoS$_2$ and (d) 2H-MoS$_2$. Experimental conditions: [FLO] = 20 mg/L, supporting electrolyte [Na_2SO_4] = 100 mM, potential = −1.2 V vs. Ag/AgCl, initial pH 5.8.

defluorination, F$^-$ release increases with potential for both phases, reaching approximately 40 % defluorination efficiency. The divergence between defluorination and dechlorination likely arises from the greater thermodynamic stability of the C–F bond relative to the C–Cl bond. Once dechlorination occurs, however, the resulting FLO-2Cl intermediate becomes susceptible to reductive defluorination on the MoS$_2$ surface. This step proceeds via reactive carbanion intermediates, ultimately yielding FLO-2Cl-F [53]. Together, these results demonstrate that MoS$_2$ electrodes can mediate defluorination at elevated potentials following an initial dechlorination step.

Further quantitative analysis of dechlorination products was conducted under conditions with and without 100 mM TBA at −1.2 V potential to identify the FLO dechlorination pathways. The quantification of these products was obtained by integrating FLO degradation data from UPLC, Cl$^-$ release data from IC, and peak area data of $C_{12}H_{15}ClFNO_4S$ (FLO-Cl, $m/z = 324.0483$) and $C_{12}H_{16}FNO_4S$ (FLO-2Cl, $m/z = 289.0749$) analyzed by HPLC-MS (see Text S9). For 1T-MoS$_2$, the proportions of FLO-Cl and FLO-2Cl increased over time (Fig. 4d). Specifically, FLO-Cl rose from 5.3 % within the first hour to 15.1 % after 4 h, and FLO-2Cl increased from 21.9 % to 68.8 % over the same period. This trend indicates a growing proportion of deep dechlorination of FLO as the reaction progressed. Upon the addition of 100 mM TBA, the overall dechlorination proportion underwent significant changes. The proportion of FLO-Cl increased to 26.8 % at one hour and to 30.7 % at 4 h, while the proportion of FLO-2Cl decreased to 5.8 % at one hour and to 27.6 % at 4 h. These alterations confirmed the main role of H* in FLO deep dechlorination on the 1T-MoS$_2$ surface. Similarly, on the 2H-MoS$_2$ electrode, the proportions of FLO-2Cl/FLO-Cl increased with time (Fig. 5e). Without TBA, the FLO-Cl ratio remained at a level of approximately 22.1−19.8 % at different time, while the FLO-2Cl ratio increased from 21.3 % at 1 h to 75.2 % at 4 h. With the addition of TBA, the FLO-Cl ratio became 29.7 % at 1 h and ca. 15 % at 4 h, and the FLO-2Cl ratio decreased to 7.2 % at 1 h but remained 53.3 % at 4 h. This high percentage of FLO-2Cl strongly suggests that deep dechlorination on the 2H-MoS$_2$ electrode primarily occurs through DET. These results are also consistent with the release rates of Cl$^-$ on 1T- and 2H-MoS$_2$ (Fig. 3c and d), where a sharp release of Cl$^-$ within the first 30 min, as a result of simultaneous detachment of the two chlorine atoms, was observed on 1T-MoS$_2$; and a gradual, less steep release of Cl$^-$, due to two-step release of chlorine atoms, over the entire reaction period, was observed on 2H-MoS$_2$. Taken together, the above observations suggest that FLO on the 2H-MoS$_2$ electrode mainly engages in a step-by-step DET dechlorination process, while on the 1T-MoS$_2$ electrode, it mainly undergoes rapid one-step H*-assisted deep dechlorination. The distinct FLO dechlorination mechanism and pathways on two MoS$_2$ electrodes were further elaborated through DFT calculations.

3.5. *Thermodynamic and kinetic insights from DFT calculations*

DFT calculations were employed to elucidate the free energy changes and energy barriers associated with different dechlorination pathways. We first optimized the relevant crystal planes of both 1T- and 2H-MoS$_2$ for FLO adsorption, also considering concurrent H$^+$ adsorption. The (101) facet of 2H-MoS$_2$ exhibited the strongest FLO adsorption energy (−5.47 eV) with a stable Cl–Mo–Mo–Cl configuration, while the (101) facet of 1T-MoS$_2$ showed the highest adsorption energy (−2.99 eV) and a similar configuration (see Text S10 and Fig. S21–S23 for details).

Fig. 6a, d depict the distinct FLO dechlorination pathways on the two MoS_2 electrodes, namely, the DET and H*-driven dechlorination reactions. For the DET mechanism, FLO's C−Cl bond accepts an electron on the Mo sites of MoS_2, forming R−C$^\bullet$ radicals that interact with a proton, eventually producing R−CH (light orange zone). Conversely, for the H* mechanism, the generated H* on the MoS_2 surface (S−H*) migrates to react with the C−Cl bond, causing the bond to break and leading to the formation of R−CH (light pink zone). The competition of H_2 production on 1T- and 2H-MoS_2 is also shown in Fig. S24, based on hydrogen gas molecule formation through the Volmer and Heyrovsky reactions [17,50].

The comparison of free energy changes across different reaction pathways for 1T-/2H-MoS_2 reveals intriguing insights. In the case of 2H-MoS_2, the co-adsorption energy of FLO stands at −4.1 eV. For the DET mechanism, the energy barriers were calculated to be 0.53 eV for the first C−Cl bond breaking and 1.60 eV for the second. Moreover, for the H* mechanism, the energy barriers became 0.80 eV for the first C−Cl bond breaking and 3.23 eV for the second. The increase in energy barriers strongly suggests DET as the more kinetically favorable dechlorination pathway on 2H-MoS_2, and that the second dechlorination step via DET was more challenging than the first step, thus becoming the rate-limiting step. This is due to the higher electron-accepting tendency of the Cl−R−Cl structure compared to the H−R−Cl structure (Fig. S25, the LUMO-HOMO analysis).

When considering 1T-MoS_2, the adsorption energy for FLO was determined to be −3.06 eV. In the case of DET, the energy barriers were calculated to be 1.94 eV for breaking the first C−Cl bond and 4.67 eV for the second. For the H*-based pathway, a similar energy barrier of 2.0 eV was observed for the first dechlorination step, and an energy barrier of 1.53 eV was observed for the second, which is not only smaller than that of the first dechlorination step but also much smaller than the energy barrier of the second dechlorination step in the DET pathway. These calculation results suggest that despite the thermodynamic feasibility of both the H* and DET pathways on 1T-MoS_2, the deep dechlorination via the H* mechanism is kinetically much faster. This fast reaction rate could be attributed to the high nucleophilicity and significant reducing capacity of H* [54,55].

The DFT calculation results align well with our experimental findings. For 2H-MoS_2, the dechlorination process is dominated by a DET mechanism, as it is kinetically favorable; further, the cleavage of the two C–Cl bonds proceeds in two steps, with the second dechlorination exhibiting a significantly higher energy barrier than the first. In contrast, for 1T-MoS_2, the H*-mediated reduction pathway prevails due to its overall lower energy barriers, enabling a rapid, one-step removal of both chlorine atoms. These mechanistic insights account for the observed differences in FLO degradation kinetics (Fig. 3), chloride release rates (Fig. 4), and the formation of dechlorinated intermediates (Fig. 5), as well as the outcomes of the H* quenching and EPR experiments (Fig. 4).

The divergent catalytic selectivity of 1T- and 2H-MoS_2 stems directly from their distinct atomic coordination and consequent electronic structures, which govern interfacial charge transfer. The metallic 1 T phase, with its octahedral coordination and polarizable Mo–S bonds (Fig. 1f, h), exhibits a high density of states at the Fermi level and negligible bandgap (Fig. S26a), forming a delocalized electron reservoir. This enables rapid surface charge exchange and kinetically promotes proton adsorption and reactive H* generation, favoring a low-barrier H*-mediated mechanism (1.53 eV).

In contrast, the semiconducting 2H phase adopts trigonal prismatic coordination, forming strong covalent S–Mo–S bonds (Fig. 1g, h). This yields a localized electronic structure with a ~1.61 eV bandgap (Fig. S26b). Under cathodic polarization, injected electrons populate these localized states, facilitating a DET pathway that targets adsorbate orbitals such as C–Cl σ* [56–58]. The pathway exclusivity is underscored by kinetic barriers: while DET is favored on 2H-MoS_2, it is kinetically prohibitive on the 1 T surface (4.67 eV energy barrier). This disparity arises from the inherent electron-shielding effect of the metallic phase and its incompatible surface electronic structure, which collectively suppress orbital-specific electron donation [59,60]. Additionally, an external electric field may differentially modulate the electrostatic potential of Mo atoms in the 1 T and 2H phases of MoS_2, thereby distinctly influencing their catalytic behavior [61].

Furthermore, the HER (Heyrovsky reaction) on the two MoS_2 electrodes was calculated to reveal its competition role (Fig. S27). The 1T-MoS_2 exhibited a lower energy barrier and more favorable free energy changes for H_2 production compared to the 2H-MoS_2. Specifically, the

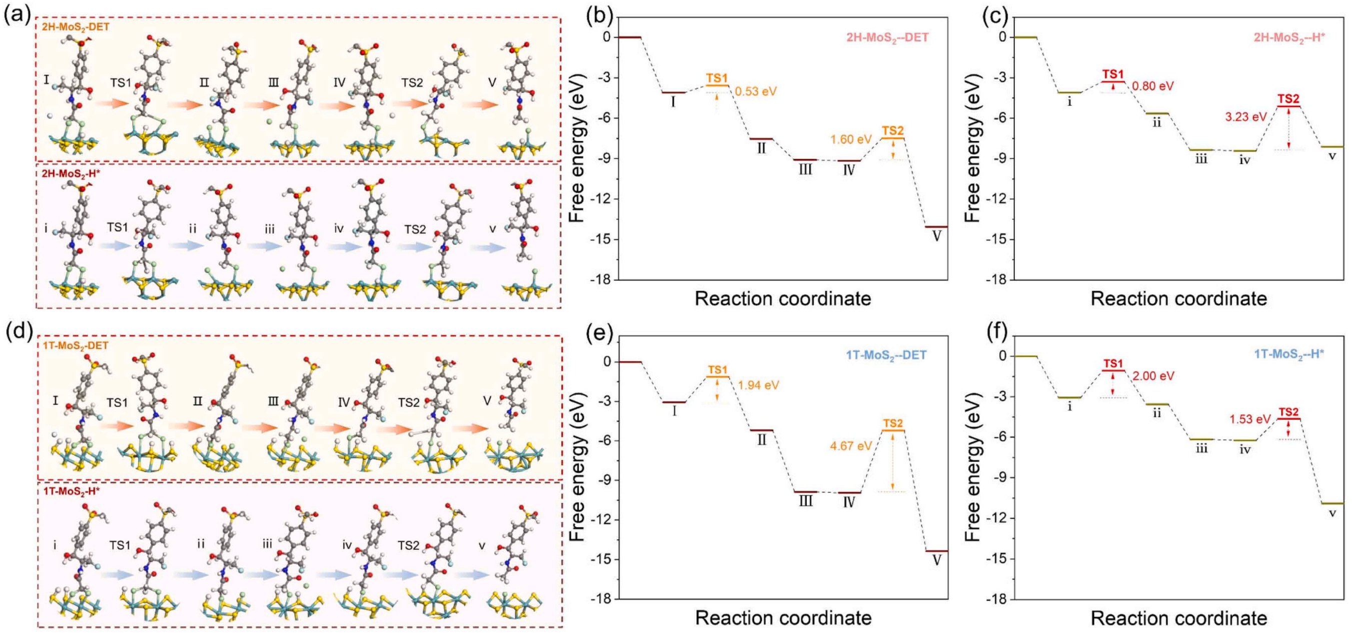

Fig. 6. DFT-calculated mechanisms of FLO dechlorination at 1T- and 2H-MoS_2 electrodes. (a) Reaction pathways on the 2H-MoS_2 phase. (b, c) Gibbs free energy profiles for dechlorination via the (b) direct electron transfer (DET) and (c) atomic hydrogen (H*) pathways on 2H-MoS_2. (d) Reaction pathways on the 1T-MoS_2 phase. (e, f) Corresponding free energy profiles for the (e) DET and (f) H* pathways on the 1T-MoS_2 electrode.

energy barrier for H* and H combination on 1T-MoS_2 was 0.55 eV, with the corresponding free energy change for H_2 formation and release being −3.71 eV and −0.05 eV, respectively. In contrast, the 2H-MoS_2 demonstrated a higher energy barrier (0.69 eV) for H_2 production and more positive free energy changes: −1.55 eV for H_2 formation and 0.39 eV for H_2 release. These results suggest that H_2 production is more thermodynamically and kinetically favorable on the 1T-MoS_2 than the 2H-MoS_2, aligning with many previous literature reports [17,62]. The lower energy barrier for H_2 production (0.55 eV) compared to FLO dechlorination (1.93 or 2.0 eV) on 1T-MoS_2 indicates faster H_2 production over FLO dechlorination, explaining its low FLO dechlorination performance at low electrical potentials. Conversely, the 2H-MoS_2 exhibited a lower energy barrier for FLO dechlorination (0.53 eV) than for H_2 production (0.69 eV), resulting in high FLO dechlorination performance at even low electrical potentials.

3.6. Stability and applicability under varying environmentally relevant conditions

Fig. S28 illustrates the effect of the initial electrolyte pH on FLO electro-dechlorination performance. For the 2H-MoS_2 electrode, the degradation of FLO exhibited a slight decrease with rising pH levels, primarily because of improved proton transport in acidic conditions when compared to alkaline environments. Conversely, the 1T-MoS_2 electrode showed a degradation rate order of pH 5.8 > pH 11.8 > pH 2.8, attributed to increased H_2 production under acidic conditions, leading to fewer H* available for FLO dechlorination. NOM at environmental concentrations of 2 or 6 mg/L had minimal impact on FLO dechlorination for both electrodes (Fig. S29a). Additionally, in actual water matrices, DO influences the performance of 1 T-MoS_2 more significantly than that of 2H-MoS_2, primarily due to the consumption of H* by DO. This represents a key constraint for the application of 1 T-MoS_2 in oxygen-containing natural waters (Fig. S29b). Compared with the 1 T phase, the DET dechlorination pathway on the edge sites of 2H-MoS_2 is less perturbed by DO, which may confer an advantage in oxygen-rich environments. Under low-DO or anaerobic conditions—such as groundwater, sediments, or anaerobic industrial wastewater—1 T-MoS_2 can effectively leverage its H*-mediated dechlorination pathway. In oxygen-rich waters (e.g., surface water), however, the inhibiting effect of DO must be considered. To further assess the durability of the MoS_2 electrodes, a 24-hour cycle test was conducted. The results in Fig. S30 presented that the 2H-MoS_2 electrode maintained approximately 95 % FLO removal after 6 cycles. Initially, the 1T-MoS_2 electrode exhibited 90 % FLO removal performance, which decreased to 80 % by the sixth cycle, likely due to H_2 bubble-induced detachment of catalysts. Those findings underscore the robust electrocatalytic performance of MoS_2 electrodes, emphasizing their environmental resilience and suitability for practical applications.

4. Conclusions

In this study, we developed a cost-effective MoS_2 electrocatalyst capable of achieving deep dehalogenation of the antibiotic FLO and elucidated the phase-dependent dechlorination mechanisms of the MoS_2 electrodes. Notably, the DET mechanism dominated deep dechlorination on 2H-MoS_2, with H* playing only a minor role. In contrast, H* contributed significantly to FLO dechlorination on 1T-MoS_2, with H* serving as the primary driver for deep dechlorination. This work clarified the distinct electrochemical dechlorination pathways on 1T- and 2H-MoS_2, offering new insights for both fundamental electrocatalytic dehalogenation research and practical applications in chlorinated antibiotic treatment. Although the reaction mechanism has been studied in detail, two fundamental challenges persist: identifying the specific active sites on the MoS_2 electrode and developing strategies to maximize the utilization of H* and electrons. To address these, future work should aim to (1) optimize Mo site exposure at edge/planar regions of MoS_2 through vacancy engineering to expand dechlorination sites for OCs and (2) introduce metal-doped sites to enhance OCs adsorption and H*/electron utilization efficiency. These structural engineering approaches are crucial for further enhancing the performance and stability of MoS_2 in electrochemical dehalogenation systems.

CRediT authorship contribution statement

Beizhao Chen: Investigation, formal analysis, data curation, calculation, conceptualization, writing; **Mengxia Wang:** Formal analysis; **Aling Wan:** Formal analysis; **Meng Zhang:** Formal analysis; **Hanchao Zhang:** Calculation methodology, **Yi Jiang:** Conceptualization, writing - review & editing, supervision, funding acquisition; and **Zhongying Wang:** Writing - review & editing, supervision, funding acquisition.

Declaration of Competing Interest

The authors declare that they have no known competing financial interests or personal relationships that could have appeared to influence the work reported in this paper.

Acknowledgements

This work was partially supported by the Co-funding Mechanism on Joint Laboratories with the Chinese Academy of Sciences sponsored by the Research Grants Council of Hong Kong JLFS/E-502/24).

Appendix A. Supporting information

Supplementary data associated with this article can be found in the online version at doi:10.1016/j.apcatb.2026.126479.

Data availability

Data will be made available on request.

References

[1] Q.-Q. Zhang, G.-G. Ying, C.-G. Pan, Y.-S. Liu, J.-L. Zhao, Comprehensive evaluation of antibiotics emission and fate in the river basins of China: source analysis, multimedia modeling, and linkage to bacterial resistance, Environ. Sci. Technol. 49 (2015) 6772–6782.

[2] S.K. Khetan, T.J. Collins, Human pharmaceuticals in the aquatic environment: a challenge to green chemistry, Chem. Rev. 107 (2007) 2319–2364.

[3] D. Kong, B. Liang, H. Yun, H. Cheng, J. Ma, M. Cui, A. Wang, N. Ren, Cathodic degradation of antibiotics: characterization and pathway analysis, Water Res. 72 (2015) 281–292.

[4] Q. Bu, B. Wang, J. Huang, S. Deng, G. Yu, Pharmaceuticals and personal care products in the aquatic environment in China: a review, J. Hazard. Mater. 262 (2013) 189–211.

[5] D. Zhang, Y. Tang, H. Liu, Z. Wang, X. Liu, H. Tang, H. Zhang, D. Wang, Y. Long, C. Liu, Electrocatalytic deep dehalogenation and mineralization of florfenicol: synergy of atomic hydrogen reduction and hydroxyl radical oxidation over bifunctional cathode catalyst, Environ. Sci. Technol. 57 (2023) 20315–20325.

[6] E.T. Martin, C.M. McGuire, M.S. Mubarak, D.G. Peters, Electroreductive remediation of halogenated environmental pollutants, Chem. Rev. 116 (2016) 15198–15234.

[7] D. Zhou, Y.-H. Luo, C.-W. Zheng, M. Long, X. Long, Y. Bi, X. Zheng, C. Zhou, B. E. Rittmann, H2-based membrane catalyst-film reactor (H2-MCfR) loaded with palladium for removing oxidized contaminants in water, Environ. Sci. Technol. 55 (2021) 7082–7093.

[8] Y. Cai, X. Long, Y.-H. Luo, C. Zhou, B.E. Rittmann, Stable dechlorination of Trichloroacetic Acid (TCAA) to acetic acid catalyzed by palladium nanoparticles deposited on H_2-transfer membranes, Water Res. 192 (2021) 116841.

[9] M. Lei, Y. Tang, H. Wang, L. Zhu, G. Zhang, Y. Zhou, H. Tang, A catalytic strategy for rapid cleavage of C-Cl bond under mild conditions: effects of active hydrogen induced by Pd nanoparticles on the complete dechlorination of chlorobenzenes, Chem. Eng. J. 419 (2021) 129510.

[10] S. Islam, A. Redwan, K. Millerick, J. Filip, L. Fan, W. Yan, Effect of copresence of zerovalent iron and sulfate reducing bacteria on reductive dechlorination of trichloroethylene, Environ. Sci. Technol. 55 (2021) 4851–4861.

[11] S. Cai, B. Chen, X. Qiu, J. Li, P.G. Tratnyek, F. He, Sulfidation of zero-valent iron by direct reaction with elemental sulfur in water: efficiencies, mechanism, and dechlorination of trichloroethylene, Environ. Sci. Technol. 55 (2021) 645–654.

[12] M.E. Casas, R.K. Chhetri, G. Ooi, K.M.S. Hansen, K. Litty, M. Christensson, C. Kragelund, H.R. Andersen, K. Bester, Biodegradation of pharmaceuticals in hospital wastewater by staged Moving Bed Biofilm Reactors (MBBR), Water Res. 83 (2015) 293–302.

[13] Z. Gu, N. Ni, G. He, Y. Shan, K. Wu, C. Hu, J. Qu, Enhanced hydrosaturation selectivity and electron transfer for electrocatalytic chlorophenols hydrogenation on Ru sites, Environ. Sci. Technol. 57 (2023) 16695–16706.

[14] Y. Min, S.-C. Mei, X.-Q. Pan, J.-J. Chen, H.-Q. Yu, Y. Xiong, Mimicking reductive dehalogenases for efficient electrocatalytic water dechlorination, Nat. Commun. 14 (2023) 5134.

[15] C. Choi, X. Wang, S. Kwon, J.L. Hart, C.L. Rooney, N.J. Harmon, Q.P. Sam, J.J. Cha, W.A. Goddard, M. Elimelech, H. Wang, Efficient electrocatalytic valorization of chlorinated organic water pollutant to ethylene, Nat. Nanotechnol. 18 (2023) 160–167.

[16] Z. Wang, B. Mi, Environmental applications of 2D molybdenum disulfide (MoS2) nanosheets, Environ. Sci. Technol. 51 (2017) 8229–8244.

[17] Y. Cao, Roadmap and direction toward high-performance MoS2 hydrogen evolution catalysts, ACS Nano 15 (2021) 11014–11039.

[18] J. Li, Y. Zhang, C. Liu, L. Zheng, E. Petit, K. Qi, Y. Zhang, H. Wu, W. Wang, A. Tiberj, X. Wang, M. Chhowalla, L. Lajaunie, R. Yu, D. Voiry, 3.4% solar-to-ammonia efficiency from nitrate using Fe single atomic catalyst supported on MoS2 nanosheets, Adv. Funct. Mater. 32 (2022) 2108316.

[19] Y. Wang, H. Ma, J. Liu, Y. Yu, S. Zuo, Micron-scale vertical MoS$_2$/porous g-C$_3$N$_4$ Piezocatalyst via a precursor’s supramolecular self-template architecture: degradation and hydrogen evolution, ACS Appl. Mater. Interfaces 16 (2024) 55325–55342.

[20] W. Chen, J. Gu, Y. Du, F. Song, F. Bu, J. Li, Y. Yuan, R. Luo, Q. Liu, D. Zhang, Achieving rich and active alkaline hydrogen evolution heterostructures via interface engineering on 2D 1T-MoS$_2$ quantum sheets, Adv. Funct. Mater. 30 (2020) 2000551.

[21] G. Li, D. Zhang, Q. Qiao, Y. Yu, D. Peterson, A. Zafar, R. Kumar, S. Curtarolo, F. Hunte, S. Shannon, Y. Zhu, W. Yang, L. Cao, All the catalytic active sites of MoS2 for hydrogen evolution, J. Am. Chem. Soc. 138 (2016) 16632–16638.

[22] P. Abbasi, M. Asadi, C. Liu, S. Sharifi-Asl, B. Sayahpour, A. Behranginia, P. Zapol, R. Shahbazian-Yassar, L.A. Curtiss, A. Salehi-Khojin, Tailoring the edge structure of molybdenum disulfide toward electrocatalytic reduction of carbon dioxide, ACS Nano 11 (2017) 453–460.

[23] K.L. Lv, C. Teng, M.H. Shi, Y. Yuan, Y. Zhu, J.R. Wang, Z. Kong, X.Y. Lu, Y. Zhu, Hydrophobic and electronic properties of the E-MoS$_2$ nanosheets induced by FAS for the CO$_2$ electroreduction to syngas with a wide range of CO/H$_2$ ratios, Adv. Funct. Mater. 28 (2018).

[24] J. Hu, L. Yu, J. Deng, Y. Wang, K. Cheng, C. Ma, Q. Zhang, W. Wen, S. Yu, Y. Pan, J. Yang, H. Ma, F. Qi, Y. Wang, Y. Zheng, M. Chen, R. Huang, S. Zhang, Z. Zhao, J. Mao, X. Meng, Q. Ji, G. Hou, X. Han, X. Bao, Y. Wang, D. Deng, Sulfur vacancy-rich MoS$_2$ as a catalyst for the hydrogenation of CO$_2$ to methanol, Nat. Catal. 4 (2021) 242–250.

[25] D.K. Perivoliotis, Y. Sato, K. Suenaga, N. Tagmatarchis, Covalently functionalized layered MoS2 supported Pd nanoparticles as highly active oxygen reduction electrocatalysts, Nanoscale 12 (2020) 18278–18288.

[26] K. Moon, H.K. Lee, Y. Park, S. Jang, H. Lim, J.C. Park, K.H. Park, A new synthesis of highly dispersed MoS$_2$ nanoparticles on ketjenblack carbon for sustainable oxygen reduction reaction, Catal. Lett. 152 (2022) 353–360.

[27] S. Ramakrishnan, M. Karuppannan, M. Vinothkannan, K. Ramachandran, O. J. Kwon, D.J. Yoo, Ultrafine Pt nanoparticles stabilized by MoS$_2$/N-doped reduced graphene oxide as a durable electrocatalyst for alcohol oxidation and oxygen reduction reactions, ACS Appl. Mater. Interfaces 11 (2019) 12504–12515.

[28] G. Lin, Q. Ju, X. Guo, W. Zhao, S. Adimi, J. Ye, Q. Bi, J. Wang, M. Yang, F. Huang, Intrinsic electron localization of metastable MoS$_2$ boosts electrocatalytic nitrogen reduction to ammonia, Adv. Mater. 33 (2021) 2007509.

[29] X. Liu, X. Xu, F. Li, J. Xu, H. Ma, X. Sun, D. Wu, C. Zhang, X. Ren, Q. Wei, Heterostructured Bi2S3/MoS2 nanoarrays for efficient electrocatalytic nitrate reduction to ammonia under ambient conditions, ACS Appl. Mater. Interfaces 14 (2022) 38835–38843.

[30] Y. Wang, Y. Xu, C. Cheng, B. Zhang, B. Zhang, Y. Yu, Phase-regulated active hydrogen behavior on molybdenum disulfide for electrochemical nitrate-to-ammonia conversion, Angew. Chem. Int. Ed. 63 (2024) e202315109.

[31] L.-Z. Huang, S.U. Pedersen, E.T. Bjerglund, P. Lamagni, M. Glasius, H.C.B. Hansen, K. Daasbjerg, Hierarchical MoS$_2$ nanosheets on flexible carbon felt as an efficient flow-through electrode for dechlorination, Environ. Sci. Nano 4 (2017) 2286–2296.

[32] M. Dauda, C. Basheer, M.H. Al-Malack, M.N. Siddiqui, Efficient Co-MoS$_2$ electrocatalyst for cathodic degradation of halogenated disinfection by-products in water sample, Sep. Purif. Technol. 259 (2021) 118085.

[33] J. Yang, S.-F. Jiang, W.-F. Hu, H. Jiang, Highly efficient electrochemical dechlorination of florfenicol by an ultrathin molybdenum disulfide cathode, Chem. Eng. J. 427 (2022) 131600.

[34] H. Zeng, G. Zhang, Q. Ji, H. Liu, X. Hua, H. Xia, M. Sillanpää, J. Qu, pH-independent production of hydroxyl radical from atomic H*-mediated electrocatalytic H$_2$O$_2$ reduction: a green fenton process without byproducts, Environ. Sci. Technol. 54 (2020) 14725–14731.

[35] L.-Z. Huang, Y. Wang, J. Deng, J. Yuan, Y. Dai, W. Yin, Generation of adsorbed atomic hydrogen by Pd(II) doped Fe(OH)$_2$ enables ultra-fast reductive dechlorination of trichloroethylene, Appl. Catal. B Environ. 322 (2023) 122094.

[36] M. Wang, Q. Han, Y. Shu, K. Wang, L. Wang, B. Liu, I. Zucker, Z. Wang, Matrix effects on the performance and mechanism of Hg removal from groundwater by MoS$_2$ nanosheets, Environ. Sci. Adv. 1 (2022) 59–69.

[37] Z. Wang, A. von dem Bussche, Y. Qiu, T.M. Valentin, K. Gion, A.B. Kane, R.H. Hurt, Chemical dissolution pathways of MoS$_2$ nanosheets in biological and environmental media, Environ. Sci. Technol. 50 (2016) 7208–7217.

[38] B. Liu, Q. Han, L. Li, S. Zheng, Y. Shu, J.A. Pedersen, Z. Wang, Synergistic effect of metal cations and visible light on 2D MoS$_2$ nanosheet aggregation, Environ. Sci. Technol. 55 (2021) 16379–16389.

[39] F. Niefind, J. Djamil, W. Bensch, B.R. Srinivasan, I. Sinev, W. Grünert, M. Deng, L. Kienle, A. Lotnyk, M.B. Mesch, J. Senker, L. Dura, T. Beweries, Room temperature synthesis of an amorphous MoS$_2$ based composite stabilized by N-donor ligands and its light-driven photocatalytic hydrogen production, RSC Adv. 5 (2015) 67742–67751.

[40] K. Sun, Y. Liu, Y. Pan, H. Zhu, J. Zhao, L. Zeng, Z. Liu, C. Liu, Targeted bottom-up synthesis of 1T-phase MoS$_2$ arrays with high electrocatalytic hydrogen evolution activity by simultaneous structure and morphology engineering, Nano Res. 11 (2018) 4368–4379.

[41] M.D. Segall, J.D.L. Philip, M.J. Probert, C.J. Pickard, P.J. Hasnip, S.J. Clark, M. C. Payne, First-principles simulation: ideas, illustrations and the CASTEP code, J. Phys. Condens. Matter 14 (2002) 2717.

[42] L. Li, Q. Han, L. Wang, B. Liu, K. Wang, Z. Wang, Dual roles of MoS$_2$ nanosheets in advanced oxidation processes: activating permonosulfate and quenching radicals, Chem. Eng. J. 440 (2022) 135866.

[43] Q. Han, J. Yu, S. Poon, L. Sun, M. Teli, B. Liu, H. Chen, K. Wang, Z. Wang, B. Mi, Highly efficient removal and sequestration of Cr(VI) in confined MoS$_2$ interlayer nanochannels: performance and mechanism, Sep. Purif. Technol. 293 (2022) 121104.

[44] S. Venkateshwaran, S.M. Senthil Kumar, Provoking metallic 1T phase conversion of 2H-MoS$_2$ via an effectual solvothermal route for electrocatalytic water reduction in acid, ACS Sustain. Chem. Eng. 10 (2022) 5258–5267.

[45] H. Su, L. Chen, Y. Chen, R. Si, Y. Wu, X. Wu, Z. Geng, W. Zhang, J. Zeng, Single atoms of iron on MoS2 nanosheets for N2 electroreduction into ammonia, Angew. Chem. Int. Ed. 59 (2020) 20411–20416.

[46] M.-R. Gao, M.K.Y. Chan, Y. Sun, Edge-terminated molybdenum disulfide with a 9.4-Å interlayer spacing for electrochemical hydrogen production, Nat. Commun. 6 (2015) 7493.

[47] H.Q. Niu, R.X. Zhao, H.Y. Yang, L.L. Tong, Y.Q. Zhou, Variations in structure and adsorption characteristics of humic acid during pressure oxidation process, Trans. Nonferrous Met. Soc. China 34 (2024) 1694–1709.

[48] N.S. van Leeuwen, S. Mathew, C.E.J. van Lare, M.P. Ahr, A. Zwijnenburg, S. Pullen, B. de Bruin, Atom transfer radical addition of activated primary alkyl chlorides using in situ generated [Cp*RuII(Cl)(PR$_3$)] catalysts, CHEMCATCHEM 16 (2024).

[49] Z. Lou, Z. Wang, J. Zhou, C. Zhou, J. Xu, X. Xu, Pd/TiC/Ti electrode with enhanced atomic H* generation, atomic H* adsorption and 2,4-DCBA adsorption for facilitating electrocatalytic hydrodechlorination, Environ. Sci. Nano 7 (2020) 1566–1581.

[50] Y. Guo, Y. Li, Z. Wang, Electrocatalytic hydro-dehalogenation of halogenated organic pollutants from wastewater: a critical review, Water Res. 234 (2023) 119810.

[51] Y. Shen, Y. Tong, J. Xu, S. Wang, J. Wang, T. Zeng, Z. He, W. Yang, S. Song, Ni-based layered metal-organic frameworks with palladium for electrochemical dechlorination, Appl. Catal. B Environ. 264 (2020) 118505.

[52] L. Hu, L. Shi, F. Shen, Q. Tong, X. Lv, Y. Li, Z. Liu, L. Ao, X. Zhang, G. Jiang, La Hou, Electrocatalytic hydrodechlorination system with antiscaling and anti-chlorine poisoning features for salt-laden wastewater treatment, Water Res. 225 (2022) 119210.

[53] Z. Chen, J. Chen, S. Tan, Z. Yang, Y. Zhang, Dechlorination helps defluorination: insights into the defluorination mechanism of florfenicol by S-nZVI and DFT calculations on the reaction pathways, Environ. Sci. Technol. 58 (2024) 2542–2553.

[54] Z. Gu, N. Ni, Y. Kang, H. Wang, W. Zhang, K. Wu, C. Hu, J. Qu, Electronic regulation of Ru electrocatalyst for enhanced atomic hydrogen generation and selective chlorophenol hydrogenation, Appl. Catal. B Environ. Energy 365 (2025) 124958.

[55] W. Zheng, Y. Liu, F. Liu, Y. Wang, N. Ren, S. You, Atomic hydrogen in electrocatalytic systems: generation, identification, and environmental applications, Water Res. 223 (2022) 118994.

[56] K.P. Dhakal, G. Ghimire, K. Chung, D.L. Duong, S.W. Kim, J. Kim, Probing multiphased transition in bulk MoS2 by direct electron injection, ACS Nano 13 (2019) 14437–14446.

[57] D. Voiry, R. Fullon, J. Yang, C. de Carvalho Castro e Silva, R. Kappera, I. Bozkurt, D. Kaplan, M.J. Lagos, P.E. Batson, G. Gupta, Aditya D. Mohite, L. Dong, D. Er, V. B. Shenoy, T. Asefa, M. Chhowalla, The role of electronic coupling between substrate and 2D MoS$_2$ nanosheets in electrocatalytic production of hydrogen, Nat. Mater. 15 (2016) 1003–1009.

[58] S. García-Dalí, J.I. Paredes, S. Villar-Rodil, A. Martínez-Jódar, A. Martínez-Alonso, J.M.D. Tascón, Molecular functionalization of 2H-Phase MoS2 nanosheets via an electrolytic route for enhanced catalytic performance, ACS Appl. Mater. Interfaces 13 (2021) 33157–33171.

[59] Y. Tan, M. Bo, Electrostatic shielding effects and binding energy shifts and topological phases of bilayer molybdenum chalcogenides, ChemistrySelect 9 (2024) e202303817.

[60] Y. Aierken, C. Sevik, O. Gülseren, F.M. Peeters, D. Çakır, In pursuit of barrierless transition metal dichalcogenides lateral heterojunctions, Nanotechnology 29 (2018) 295202.
[61] C. Cai, T. Jiang, H. Peng, X. Fu, C. Nie, Z. Ao, Sustainable peroxymonosulfate activation by 1T/2H-MoS_2 cathode for enhanced removal of organic pollutants: performance and nonradical activation mechanism based on surface Mo-peroxymonosulfate complexes, Chem. Eng. J. 518 (2025) 164474.
[62] Y. Yin, J. Han, Y. Zhang, X. Zhang, P. Xu, Q. Yuan, L. Samad, X. Wang, Y. Wang, Z. Zhang, P. Zhang, X. Cao, B. Song, S. Jin, Contributions of phase, sulfur vacancies, and edges to the hydrogen evolution reaction catalytic activity of porous molybdenum disulfide nanosheets, J. Am. Chem. Soc. 138 (2016) 7965–7972.